ROYAL SOCIETY
OF CHEMISTRY

Origin of photoelectrochemical CO_2 reduction on bare Cu(In,Ga)S$_2$ (CIGS) thin films in aqueous media without co-catalysts†

Rajiv Ramanujam Prabhakar, ‡[ae] Sudhanshu Shukla, ‡*[bcd] Haoyi Li, [ae]
R. Soyoung Kim,[e] Wei Chen, [f] Jérôme Beaudelot, [cg] Jan D'Haen, [d]
Daniely Reis Santos, [bcd] Philippe M. Vereecken, [cgh] Gian-Marco Rignanese, [fi]
Ethan J. Crumlin, [ej] Junko Yano, [ak] Bart Vermang [bcd] and
Joel W. Ager III *[aelm]

Photoelectrochemical (PEC) CO_2 reduction (CO_2R) on semiconductors provides a promising route to convert CO_2 to fuels and chemicals. However, most semiconductors are not stable under CO_2R conditions in aqueous media and require additional protection layers for long-term durability. To identify materials that would be stable and yield CO_2R products in aqueous conditions, we investigated bare Cu(In,Ga)S$_2$ (CIGS) thin films. We synthesized CIGS thin films by sulfurizing a sputtered Cu–In–Ga metal stack. The as-synthesized CIGS thin films are Cu-deficient and have a high enough bandgap (1.7 eV) suitable to perform CO_2R. The bare CIGS photocathodes had faradaic yields of 14% for HCOO$^-$ and 30% for CO in 0.1 M KHCO$_3$ electrolyte without the use of any co-catalysts under 1 sun illumination at an applied bias of -0.4 V *vs.* RHE and operated stably for 80 min. *Operando* Raman spectroscopy under CO_2R conditions showed that the dominant A$_1$ mode of CIGS was unaffected during operation. Post-mortem X-ray photoelectron spectroscopy (XPS) and X-ray absorption spectroscopy (XAS) analysis suggests that the CO_2R stability could be related to self-protection caused by the *in situ* formation of oxides/hydroxides of Ga and In during operation. Density functional theory (DFT) calculations also reveal that Ga and In are the preferential sites for the adsorption of CO_2R products, particularly HCOO$^-$. These results show that CIGS is a promising semiconductor material for performing direct semiconductor/electrolyte reactions in aqueous media for the PEC CO_2R.

Broader context

Artificial photosynthetic systems use sunlight to convert CO_2 to value added products. These are photoelectrochemical (PEC) devices that rely on semiconductor–electrolyte junctions. However, very few photocathode semiconductor materials are stable and yield CO_2 reduction (CO_2R) products without any protection layers and/or co-catalysts in aqueous media. This severely limits the artificial photosynthesis community from investigating direct semiconductor–electrolyte reactions and exploiting the rich interface chemistry relevant to PEC CO_2R. Herein, we show stable PEC CO_2R operation (>1 h)

[a] *Liquid Sunlight Alliance, Lawrence Berkeley National Laboratory, Berkeley, California 94720, USA. E-mail: jwager@lbl.gov*

[b] *Imec, Imo-imomec, Thor Park 8320, 3600, Genk, Belgium. E-mail: sudhanshu.shukla@imec.be*

[c] *EnergyVille, Thor Park 8320, 3600, Genk, Belgium*

[d] *Hasselt University, Institute for Materials Research (imo-imomec), Analytical & Microscopical Services (AMS), Martelarenlaan 42, B-3500 Hasselt, Belgium*

[e] *Chemical Sciences Division, Lawrence Berkeley National Laboratory, Berkeley, California 94720, USA*

[f] *UCLouvain, Institut de la Matière Condensée et des Nanosciences (IMCN), Louvain-la-Neuve, 1348, Belgium*

[g] *Imec Leuven Kapeldreef 75, 3001, Leuven, Belgium*

[h] *KU Leuven, M²S, cMACS, Celestijnenlaan 200F, 3001, Leuven, Belgium*

[i] *WEL Research Institute, 1300 Wavre, Belgium*

[j] *Advanced Light Source, Lawrence Berkeley National Laboratory, Berkeley, California, 94720, USA*

[k] *Molecular Biophysics and Integrated Bioimaging Division, Lawrence Berkeley National Laboratory, Berkeley, California, 94720, USA*

[l] *Department of Materials Science and Engineering, University of California, Berkeley, Berkeley, CA 94720, USA*

[m] *Materials Sciences Division, Lawrence Berkeley National Laboratory, Berkeley, California, 94720, USA*

† Electronic supplementary information (ESI) available. See DOI: **https://doi.org/10.1039/d4ey00233d**

‡ Equal contribution.

on Cu(In,Ga)S$_2$ (CIGS) based photocathodes in aqueous media without any protection layer or co-catalyst. We combined operando spectroelectrochemical measurements, advanced photoelectron spectroscopy and computational methods to investigate the underlying reasons for the catalytic activity and aqueous stability. We found that Ga and In sites provide favorable binding energy for the CO$_2$R intermediates and the formation of oxide/hydroxide species at the surface acts as self-passivation, improving the stability in aqueous media. A stable photocathode yielding > 40% faradaic efficiency for CO$_2$R products (14% for HCOO$^-$ and 30% for CO) without any co-catalysts in aqueous media has rarely been reported previously. These results emphasize the importance of previously unexplored surface compositions and/or specific defects in CIGS. This work guides the community to discover other semiconductors that are catalytically active and stable under aqueous PEC CO$_2$R conditions.

Introduction

As shown in Scheme 1, there are two main configurations in which photoelectrochemical (PEC) CO$_2$ reduction (CO$_2$R) on semiconductor materials can be accomplished: (1) *via* a direct semiconductor/electrolyte interface or (2) with a buried junction, *i.e.*, a semiconductor with protection layers/co-catalysts. The main distinction between the two configurations is that in (1) the semiconductor absorbs light, generates an electron–hole pair and intrinsically performs catalysis, while in (2) the semiconductor is not directly involved in the catalytic reaction. While configuration (2) has been extensively investigated to accomplish PEC CO$_2$R,[1–6] very few reports exist concerning configuration (1). The major bottleneck for a direct scheme is the scarce availability of stable (corrosion resistant) light-absorbing semiconductor materials under CO$_2$R conditions in aqueous media.[7] Among very few examples, Mg-doped CuFeO$_2$ has been reported for configuration (1).[8] However, the catalytic activity was attributed to the presence of metallic Cu on the surface rather than to the semiconductor itself.

There are reports on materials like Cu$_2$O and Cu(In,Ga)S$_2$ (CIGS) that do show CO$_2$R products (CO, HCOO$^-$), but they have been investigated in non-aqueous media due to long-term stability concerns.[9,10] Chalcopyrite Cu(In,Ga)Se$_2$ (CIGSe) with a CdS electron transport layer has been reported to be active for PEC CO$_2$R when a molecular coating is used to limit Cd corrosion.[11] However, there are no reports on using these bare materials (configuration (1)) for PEC CO$_2$R in aqueous electrolyte. Therefore, the quest for an intrinsically stable semiconductor (that is, without protection layers or co-catalysts) that can perform PEC CO$_2$R in aqueous media is still on.

Examination of the photocatalysis literature suggests that sulfide-based semiconductors could be promising for configuration 2.

Interestingly, CuGaS$_2$, (CuGa)$_{0.5}$ZnS$_2$, (AgInS$_2$)$_x$–(ZnS)$_{2-2x}$, Ag$_2$ZnGeS$_4$, Ni- or Pb-doped ZnS, (ZnS)$_{0.9}$–(CuCl)$_{0.1}$, and ZnGa$_{0.5}$In$_{1.5}$S$_4$ have shown promise in a particulate Z-scheme architecture with the aid of electron donors and an electron extracting layer like a reduced graphene oxide-TiO$_2$ composite for the production of CO and HCOO$^-$.[12–14] Cu$_2$ZnSnS$_4$ (CZTS) has been reported to show PEC CO$_2$R products like CO in configuration (1), but with very low photocurrents (<100 μAcm^{-2}).[15] Furthermore, Cu$_2$ZnGeS$_4$ (CZGS) thin films have shown CO production by PEC CO$_2$R, but the faradaic efficiencies (FEs) were quite low (<3%).[16]

Cu(In,Ga)S$_2$ (CIGS) is a non-toxic material that has been gaining attention recently for direct semiconductor/electrolyte (configuration (1)) photoelectrochemical (PEC) CO$_2$R, with a reported FE of ∼80% for CO$_2$R in non-aqueous electrolytes.[17] However, CIGS films investigated to date under aqueous conditions have yielded very low (<4%) FE towards CO$_2$R products like CO.[9] The underlying causes of the aqueous instability and poor catalytic performance of the reported films are not clear. Recently, wide-bandgap (1.6 eV) Cu-deficient CIGS films have shown higher quasi-Fermi level splitting (qFLS) and carrier lifetime compared to stoichiometric and Cu-excess CIGS composition films, resulting in improved photovoltaic efficiencies.[18,19] These considerations motivated us to investigate CIGS thin film photocathodes with even higher bandgaps (∼1.77 eV) and an intentionally highly Cu-deficient surface composition to have low intrinsic carrier losses. Moreover, a low Ga content (10–30%) in CIGS preserves the phase stability while providing a conduction band position high enough for PEC CO$_2$R.

In this work, we show that CIGS designed following these principles is stable under PEC CO$_2$R operation without the aid of co-catalysts or protection layers in an aqueous medium. CIGS photocathodes yielded CO$_2$R products like CO and HCOO$^-$ with a total FE of > 40%. Using *operando* Raman spectroscopy, CIGS
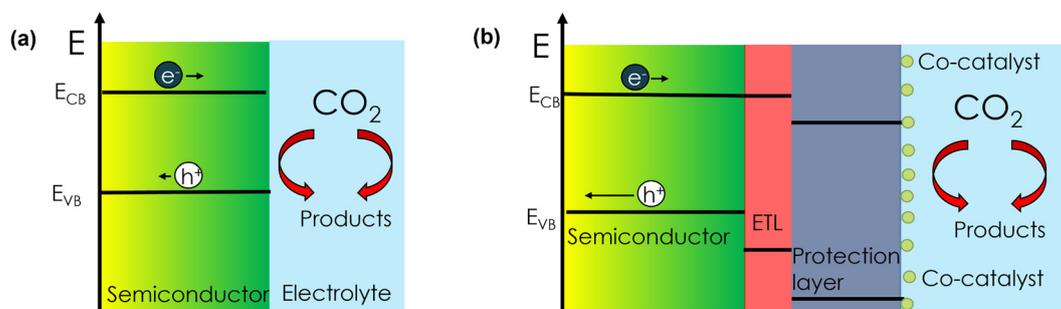
Scheme 1 (a) Configuration (1) direct semiconductor/electrolyte for PEC CO$_2$R. (b) Configuration (2) buried semiconductor for PEC CO$_2$R. (Band bending is omitted for simplicity).

thin films were shown to be stable under PEC CO_2R operation (under illumination, -0.4 V *vs.* RHE and 0.1 M $KHCO_3$) as evidenced by the persistence of the A_1 Raman mode for 30 min. We observed the formation of hydroxides/oxides of Ga and In after operation using X-ray photoelectron spectroscopy (XPS) and X-ray absorption spectroscopy (XAS), which suggests the presence of self-passivating layers. We further identified the Ga and In sites as being favorable for the adsorption of the CO_2R reaction intermediates (COOH* and *HCOO) using density functional theory (DFT) calculations. Additionally, the Cu deficiency on the CIGS surface further enhanced intermediate binding energies. Thus, CIGS films with appropriate composition and bandgap provide a viable route for direct PEC CO_2R in aqueous media.

Results and discussion

Synthesis and material characterization of CIGS thin films.

CIGS thin films were synthesized on Mo substrates by annealing a sputtered Cu–In–Ga metal stack in a H_2S atmosphere (see experimental details, synthesis of CIGS thin films). We performed X-ray diffraction (XRD) and Raman spectroscopy to analyze the phase and Ga alloying. XRD reveals the highly crystalline chalcopyrite phase to be predominant in the film. All the diffraction peaks could be indexed to the tetragonal chalcopyrite structure of CIGS (space group $I\bar{4}2d$) along with additional minor peaks at $\sim 13.3°$ and $27.3°$, which were identified as the layered $NaInS_2$ phase (Fig. 1(a)),[20] which is associated with the out-diffusion from the soda-lime glass substrate.[21–24] The alloying of the $CuInS_2$ lattice with smaller Ga atoms results in a shift of the XRD peak towards higher angles following Vegard's law. A shift of $0.4°$ corresponds to a [Ga/Ga + In] ratio (GGI) of ~ 0.3 (Fig. S1, ESI†) close to the elemental composition determined from EDX analysis, *i.e.*, $Cu_{0.7}In_{0.76}Ga_{0.24}S_2$ (Table S1, ESI†). A high degree of Cu-deficiency (*ca.* 30%) is clearly notable from composition measurement.

We further investigated the phases present in the film using Raman spectroscopy. All Raman features are assigned to the chalcopyrite CIGS phase with no evidence of binary oxide or sulfide impurity phases. However, we note that the peak overlap between the $NaInS_2$ and CIGS phases precludes their delineation using Raman spectroscopy.[20] Fitting the Raman spectra yields the predominant A_1 mode (296 cm^{-1}) and additional modes at 250, 264, 339, and 363 cm^{-1} corresponding to $E_3(TO)$, $E_3(LO)$, $E_1(TO)/B_2(TO)$, and $E_1(LO)/B_2(LO)$ vibrational modes, respectively.[25–27] For pure $CuInS_2$ and $CuGaS_2$, the A_1 mode normally appears at 291 and 311 cm^{-1}, respectively (Fig. 1(b)). The peak shift of 5 cm^{-1} compared to the pure CIS phase corresponds well to the GGI of 0.3.[25] The bandgap (E_g) value of ~ 1.77 eV, as determined from photoluminescence (PL) measurements, is close to the expected value of E_g for the measured [Ga]/[Ga + In] (GGI) ratio of ~ 0.3 (Fig. 1(c) and Fig. S1(b), ESI†).[25] We observed a broad deep defect emission below 0.5 eV from the
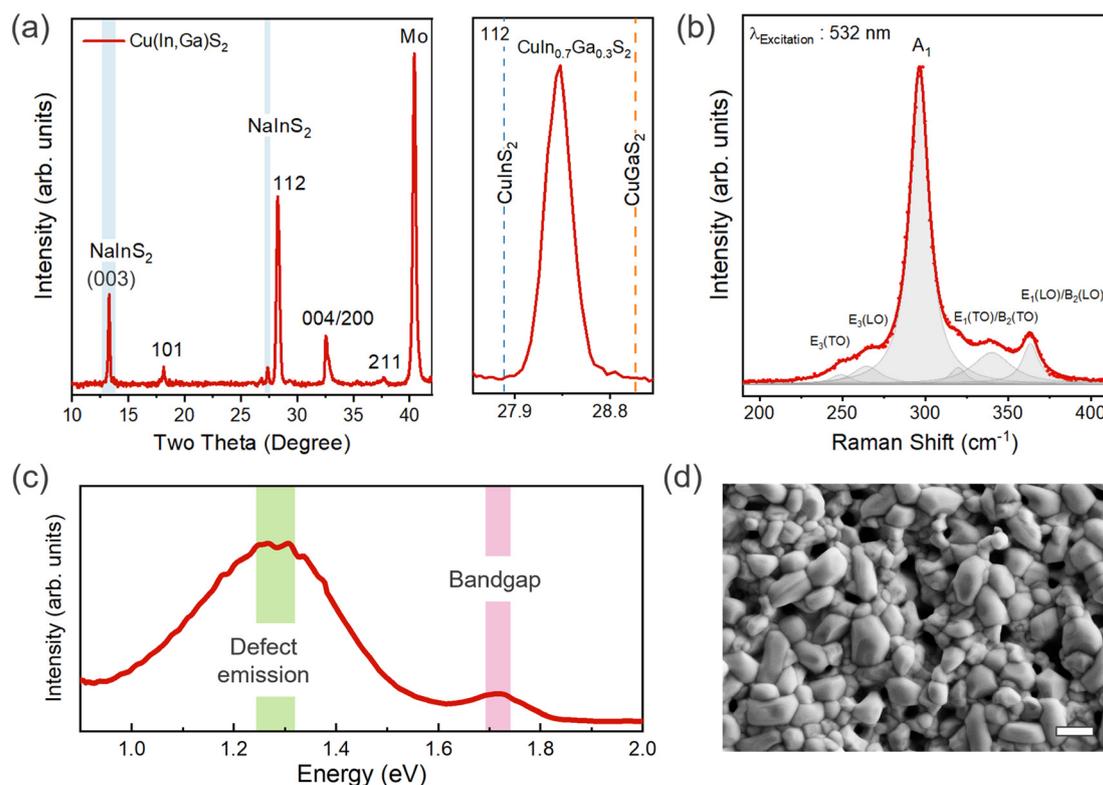

Fig. 1 (a) XRD diffractograms and (b) Raman spectrum of the CIGS thin film, (c) PL from a wide spectral range showing a bandgap at ~ 1.77 eV and broad emission at ~ 1.3 eV corresponding to deep defect(s), and (d) SEM image of the CIGS thin film showing the surface morphology. Scale bar: 1 μm.

band-edge, which has been attributed to anti-site defects (Cu_{In}/In_{Cu} or Cu_{Ga}/Ga_{Cu}) in previous studies (Fig. 1(c)).[19,25] The degree to which these anti-site defects are present in the film is predominantly governed by the cation ratio or the degree of copper off-stoichiometry. For instance, In_{Cu} and Ga_{Cu} anti-site defects are more likely to form in a Cu-deficient film.

Examining the surface from scanning electron microscopy (SEM), we observed a coarse-grained polycrystalline film with a dense array of large and small grains having an average size of ~ 1 μm (Fig. 1(d)). The sulfurization process promotes rapid grain growth governed by complex elemental interdiffusion and out-diffusion processes, while the growth kinetics determine the elemental distribution and microstructure. Consequently, voids appear at the Mo back contact due to the alkali out-diffusion process (Fig. 2(a)), with some Mo also converted to MoS_2. Similar to selenide counterparts, this interfacial MoS_2 ($MoSe_2$ in the case of CIGSe) layer might be contributing to the mechanical robustness of the interface (passing the common tape peel tests) and efficient charge extraction.[28,29] The thickness of CIGS is determined to be ~ 1.5 μm from cross-section SEM. Atomic force microscopy (AFM) analysis further confirms the high surface roughness of the CIGS film (Fig. 2(b)), noting that high surface roughness is desirable for catalytic applications as it can provide more active sites. However, we would like to mention that the pinhole formation and high surface roughness is a characteristic feature of the two-step growth process (metal stack followed by sulfurization).[30–33] In addition to well-defined CIGS grains, patches of $NaInS_2$ phase were observed at the surface as contrast in the backscattered electron image (Fig. S2, ESI†).

We performed secondary-ion mass spectroscopy (SIMS) analysis to probe the elemental composition as a function of depth. Fig. 2(c) shows slightly higher Ga at the Mo back contact and lower Cu at the front surface. This is consistent with the typical two-step growth processes for CIGS film preparation.[30,34,35] Additionally, a higher Na level at the surface might be correlated to the $NaInS_2$ phase previously observed in XRD. Further affirmation regarding the $NaInS_2$ comes from the phase analysis using electron backscattered diffraction (EBSD). Fig. 2(d) shows the patches of the $NaInS_2$ phase at the surface indicated in solid red species, while the rest of the chalcopyrite CIGS phase is shown in green. The red dots also appear in the CIGS bulk as some peak overlap occurred with the CIGS phase, sometimes causing mis-indexation (also the wrong phase and thus shown as red spots in the CIGS layer). The surface $NaInS_2$ phase is also evident in the energy-dispersive X-ray (EDX) mapping analysis (Fig. 2(e)). Nevertheless, EBSD reveals that a significant proportion of the surface is dominated by CIGS.

PEC performance of CO_2R on bare CIGS thin films in aqueous conditions

The PEC CO_2R activity of bare CIGS thin films without any protection layers or co-catalysts were examined in both N_2- and CO_2-saturated 0.1 M $KHCO_3$ aqueous media under 1 sun illumination by linear sweep voltammetry (LSV) (Fig. 3(a)). A higher photocurrent density from LSV in the case of CO_2-saturated electrolyte confirms that the observed photocurrent from the Mo/CIGS photocathode originates from photoelectrochemical reduction of CO_2. The photocurrent density typically lies within the 1.5–7 mA cm^{-2} range, with most around 3 mA cm^{-2}, for CIGS-family photocathodes reported in the literature (see summary of photocurrent density in Table S2, ESI†). Therefore, the photocurrent density of 2.8 mA cm^{-2} observed in this study is consistent with prior reports. Note that the photocurrent density takes into account the dark current of 0.4 mA cm^{-2} (Fig. 3(a)). The onset potential was observed at ~ 0.05 V vs. RHE, and the photocurrent density stabilized at ~ 1.5 mA cm^{-2} with very low dark current (0.3 mA cm^{-2}) at -0.4 V vs. RHE (Fig. 3(b)) after a rapid drop from an initial value of ~ 3.5 mA cm^{-2}. We attribute the photocurrent decay at the start of the measurement to the double layer charging effect
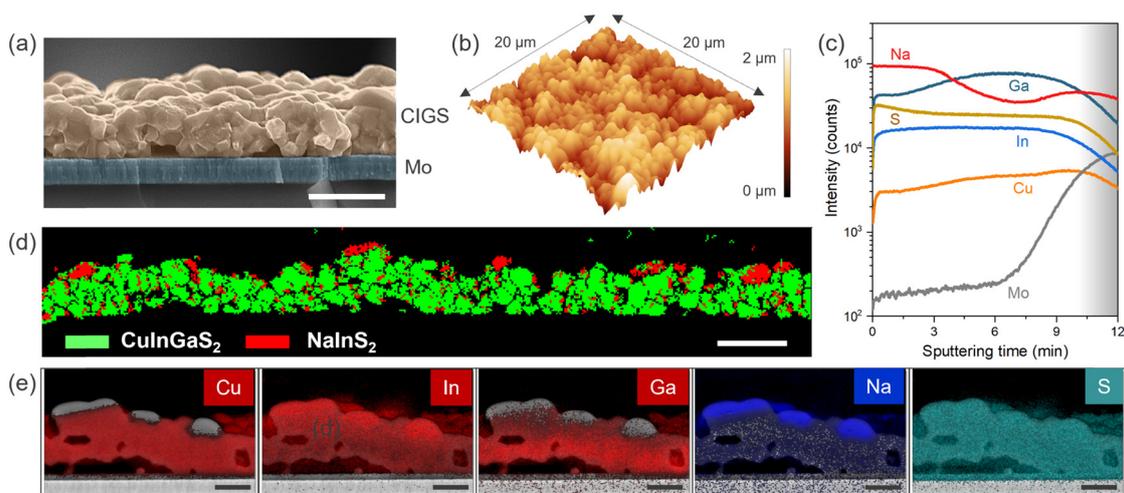

Fig. 2 (a) Cross-section SEM micrograph, scale bar: 2 μm, (b) AFM surface morphology 3D view, and (c) elemental depth profiles (Cu, In, Ga, S, Na, and Mo) from SIMS analysis of the Mo-coated glass substrate, (d) cross-section EBSD false color plot to indicate qualitative distribution and area fraction of the CIGS (in green) and $NaInS_2$ (in red) phase present in the sample. Scale bar: 2 μm. (e) Corresponding EDX mapping of the respective elements (Cu, In, Ga, Na, and S) showing the preferential segregation of Na at the surface. Scale bar: 1 μm.

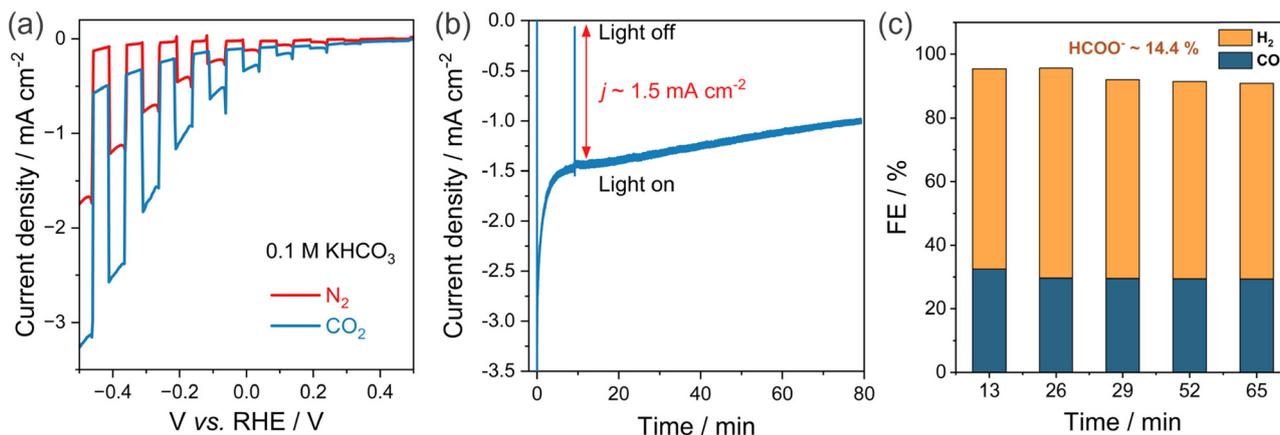**Fig. 3** PEC testing of the bare CIGS photocathode. (a) Current density *vs.* potential under 1 sun chopped light measured in N_2- and CO_2-saturated electrolyte. (b) Current density *vs.* time at -0.4 V *vs.* RHE for CO_2-saturated electrolyte. (c) Time evolution of FE for CO and H_2 at -0.4 V *vs.* RHE. CO_2 saturated 0.1M $KHCO_3$ electrolyte, 1 sun simulated AM1.5G illumination. FE < 0.3% for gaseous products like methane and ethylene. FE < 1% for liquid products such as methanol, ethanol, and other C_{2+} oxygenates.

resulting from the sudden change from open-circuit voltage (OCV) to an applied potential of -0.4 V *vs.* RHE.

The final products were individually analyzed and quantified using high precision GC and NMR measurements. A stable evolution of gaseous products (CO and H_2) was observed for 80 min under 1 sun illumination at -0.4 V *vs.* RHE (Fig. 3(c)). Although the photocurrent density decreased slowly, the FEs for CO and H_2 remained steady at around 28–32% and 60–65%, respectively. $HCOO^-$, produced with a FE of 14%, was the sole observed liquid product, and the total FE (combining CO, H_2, and $HCOO^-$) was close to unity within experimental error. Methane and ethylene were not detected (FE < 0.3%). No liquid products (*e.g.* methanol, ethanol, other C_{2+} oxygenates) were detected by sensitive NMR measurements (FE < 1%). As discussed in the previous section, the measured photocurrent density is consistent with the reported values observed for typical wide bandgap CIGS photocathodes in the literature.[17,36–40] The pinholes at the back contact might cause low photocurrents in the samples. Recent studies on high quality $CuInGaS_2$ thin films from different synthesis routes, such as a

co-evaporation process,[19,41] can guide in terms of better adhesion and morphology, and consequently photocurrents can be further improved.

Origin of CIGS surface activity and degradation probed by *in situ*/*operando* Raman spectroscopy and postmortem XPS and XAS

To characterize the structural transformation of the surface during PEC operation, we utilized surface-sensitive *operando* Raman spectroscopy and further carried out synchrotron-based X-ray photoelectron spectroscopy (XPS) and soft X-ray absorption spectroscopy (XAS) analysis of the post-mortem CIGS. In *operando* Raman spectroscopy, changes in the spectral features of the characteristic vibration modes act as markers of degradation, and the evolution of peaks provides insights on the reaction mechanism.[42]

Fig. 4 shows the Raman spectra of CIGS thin films under PEC CO_2R operation (0.1 M $KHCO_3$ at -0.4 V *vs.* RHE) where the Raman laser (2.33 eV) was used as the illumination source
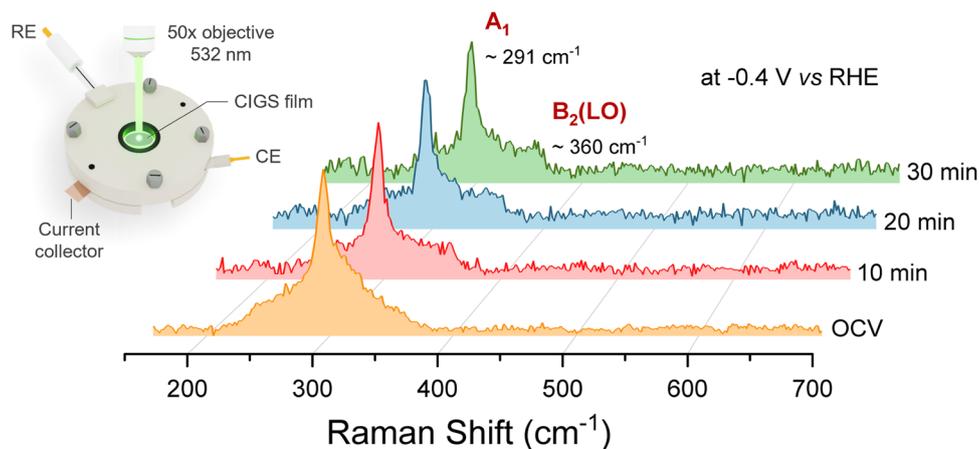

Fig. 4 *Operando* Raman spectra showing the time evolution of the CIGS photocathode under CO_2R operation at -0.4 V *vs.* RHE in CO_2-saturated 0.1 M $KHCO_3$.

for a duration of more than 30 min starting from open-circuit voltage (OCV). No noticeable change in the spectroscopic A_1 signature mode (291 cm^{-1}) of CIGS was observed in the *operando* Raman spectra for the CIGS photocathodes, indicating that the photocathodes were stable under CO_2R conditions. An additional peak at 350–360 cm^{-1} evolves as a shoulder in the Raman spectra. A signature in this spectral range is assigned to CIGS B_2(LO) mode,[17,25,39,43] as also evident in Fig. 1b. However, the reason behind the change in relative intensity of these modes during the measurements is not clear. The negligible changes in the microstructure of the photocathode before and after operation further corroborate the corrosion resistance of CIGS films under aqueous light-driven CO_2R conditions (SEM images in Fig. S3, ESI†). In contrast, the photoelectrochemical activity of $Cu_{0.84}InGa_{0.26}(S,Se)_2$ (CIGSSe) samples decreased rapidly in similar CO_2R tests concomitant with the Raman peaks completely disappearing during *operando* measurements (Fig. S4, ESI†).

We conducted post-CO_2R XPS measurements to elucidate the surface chemical changes and stability mechanisms in CO_2R. The deconvoluted Ga $2p_{3/2}$ spectrum is depicted in Fig. 5(a). In addition to the peak corresponding to Ga–S bonding in the original CIGS,[44,45] a Ga–O bonding peak (1118.5 eV) also appeared,[46–48] which significantly increased after CO_2R. Compared to the fresh CIGS, the Ga 3s photoelectron peak in CIGS after CO_2R shifted by 0.4 eV to a higher binding energy (Fig. 5(b)), further suggesting the oxide formation during CO_2R.[10] Additionally, the curve fitting results of the In $3d_{5/2}$ region show the further generation of hydroxide (445.2 eV)[17,18] from CO_2R (Fig. 5(c)). The XPS signature of In–S bonding in CIGS overlaps with In–O bonding in In_2O_3 at 444.6 eV. The apparent broadening of the In–S/In–O peak after CO_2R might imply the formation of oxide species. Under CO_2R conditions, surface-enriched In components tended to be reduced, forming In metal, as evidenced by the emerging peak at 443.5 eV after CO_2R (Fig. 5(c)).[49–51] The oxides/hydroxides formation of Ga and In likely plays a crucial role in CO_2R, enhancing the stability of CIGS through self-protection.[52–54] Furthermore, the Cu and S 2p regions remained unchanged during electrocatalysis, implying that Ga and In serve as the catalytic active sites.

The CIGS photocathodes before and after CO_2R catalysis were also examined by soft X-ray absorption spectroscopy (XAS) in the surface-sensitive total electron yield (TEY) mode. The changes in the Ga L_3-edge spectrum after CO_2R, compared with the spectra of Ga_2S_3 and Ga_2O_3 (Fig. S5(a), ESI†), were consistent with oxide formation as suggested by XPS. On the
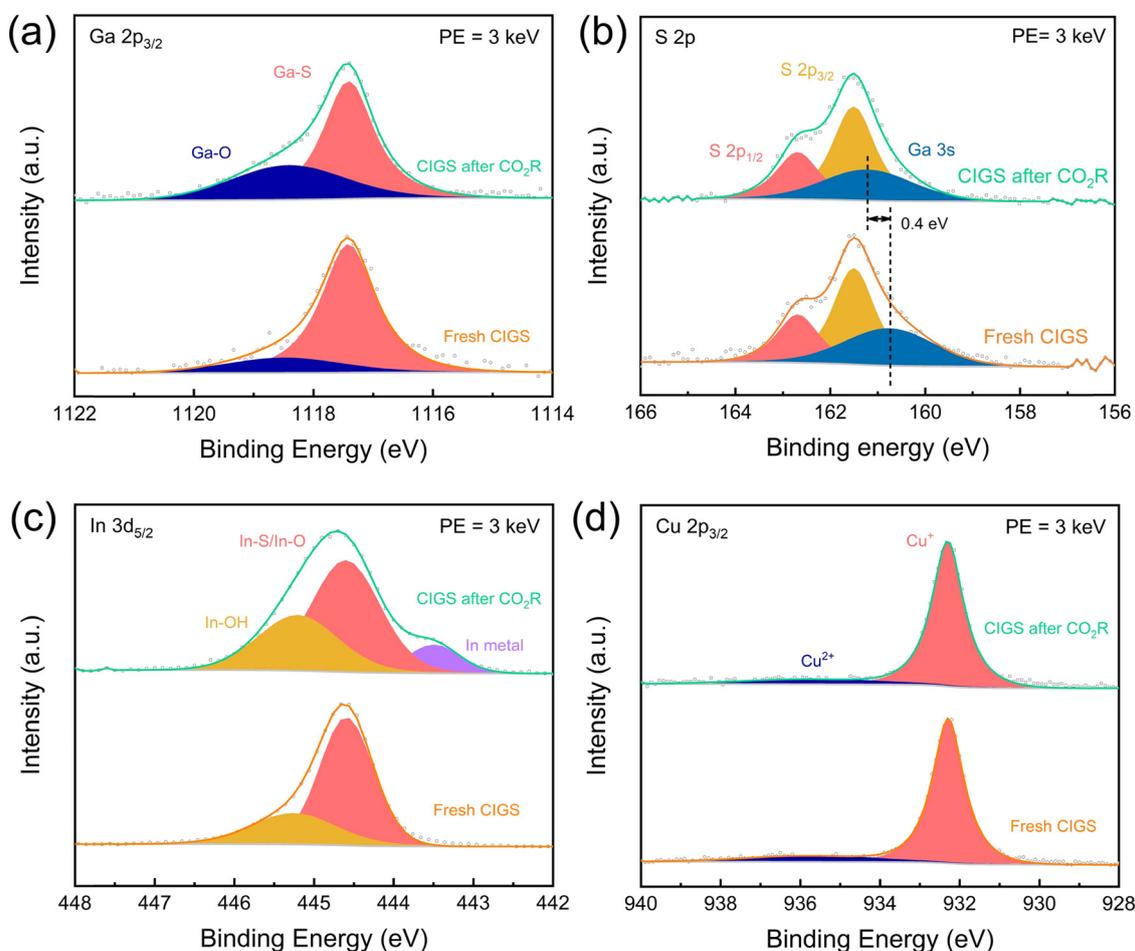

Fig. 5 Deconvoluted XPS spectra on the CIGS before and after 80 min of CO_2R operation. (a) Ga $2p_{3/2}$, (b) S 2p, (c) In $3d_{5/2}$, and (d) Cu $2p_{3/2}$ photoelectron peaks and curve fitting results (solid color area) of the fresh CIGS (bottom) and CIGS after CO_2R (upper), respectively (photon energy = 3 keV).

other hand, the In $M_{5,4}$-edge spectrum of CIGS did not change much after CO_2R (Fig. S5(b), ESI†), but the slight shift to lower energies is consistent with the formation of small amounts of In metal observed by XPS.

Computational studies of adsorption energies: affinity of CO_2R reaction intermediates on the CIGS surface

Based on the experimental realization of CIGS photocathodes, we turned to density-functional theory (DFT) to understand the atomistic origin of CO_2R on the CIGS. The PBE0 hybrid functional admixing a fraction of Fock exchange ($\alpha = 1/4$) was used in the framework of the projector-augmented wave method as implemented in VASP.[55–58] The long-range van der Waals interactions were included by the DFT+D3 method of Grimme et al.[59] The pristine CIGS(112) surface was modeled by a six-layer $CuIn_{0.75}Ga_{0.25}S_2$ slab in a tetragonal supercell comprising 192 atoms, as shown in Fig. S6 (ESI†). The In/Ga disorder is accounted for by the special quasi-random structure technique, which mimics the correlation function of a perfectly random structure.[60] Specifically, the top surface layer contains six In and two Ga atoms, thereby respecting the overall stoichiometry. A vacuum of a thickness of 15 Å separates the slab from its nearest periodic image along the z direction. Upon structural relaxations, surface Ga and In atoms can undergo sizable displacement towards vacuum by 1.7 Å from their bulk positions. As a result of this outward displacement, the surface states originating from undercoordination are passivated. Hereafter, these buckled atoms are referred to as Ga* and In* to distinguish them from their counterparts that largely remain at their bulk crystalline positions. To take into account the Cu-deficient condition, a Cu vacancy is created at the surface layer, and we limit the adsorption site of the CO_2R intermediates

to the second-nearest neighbor to the Cu vacancy. The electrochemical conversion of CO_2 to CO and formate is believed to proceed via the bound carboxylate (COOH*) and bound formate (HCOO*) intermediate, respectively.[61,62] In the subsequent section, we discuss the affinity of these CO_2R intermediates on the CIGS surface through free energy calculations following the computational hydrogen electrode method.[63] The calculations are facilitated by workflows created with the atomate2[64] and jobflow[65] frameworks. More computational details are described in the ESI.†

The calculated Gibbs free energies of change upon adsorption (ΔG) indicate that, on both pristine and Cu-deficient surfaces, the buckled Ga* site is the primary binding site to carboxyl COOH*, the intermediate for CO_2R reaction to CO, as shown in Fig. 6(a). The adsorption is mediated through the formation of the Ga*–C bond, which leads to a less prominent buckling of the Ga* atoms [cf. Fig. 6(c) and (d)]. By contrast, the ΔG is 0.6 eV higher for adsorptions on the In* site and over 2 eV higher on the Cu site. In particular, our DFT calculations show that the presence of a Cu vacancy largely stabilizes the COOH* adsorption, the effect of which is the most visible for adsorbates on the unbuckled Ga and In atoms due to their proximity to the vacancy. Nevertheless, the ΔG remains the lowest on the Ga* site, irrespective of Cu deficiency. The predominant role of the Ga* site is also confirmed for the adsorption of HCOO*, the intermediate that generally leads to the production of formate. The binding is stronger compared to the COOH* adsorption via the bridge-bonded configuration shown in Fig. 6(e).

Overall, the ΔG values obtained with the hybrid-functional calculations corroborate the XPS and XAS assignments in that the CO_2R occurs primarily through the Ga atoms and, to some extent, through the In atoms. On the other hand, we note that the enhanced catalytic activity observed under Cu-deficient
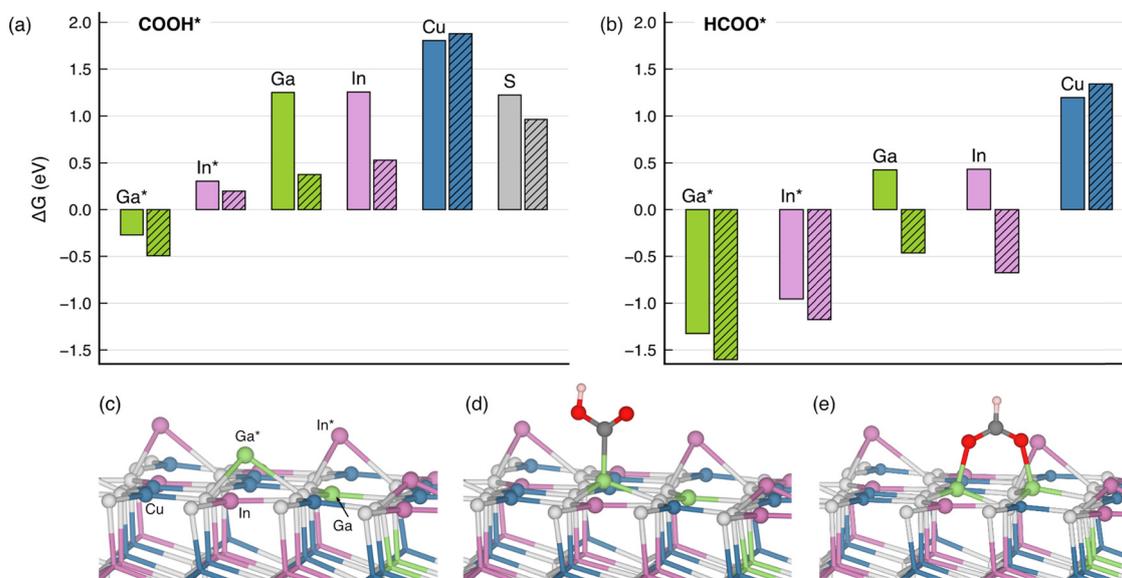

Fig. 6 Gibbs free energy of change for the adsorption of (a) COOH* and (b) HCOO* intermediates on the pristine (solid bar) and the Cu-deficient CIGS (112) surface (shaded bar). The free energies are assessed at room temperature. The adsorption on the Cu-deficient CIGS surface occurs at the sites in the close vicinity of a surface Cu vacancy. (c) illustrates the atomic structure of the Cu-deficient CIGS (112) surface prior to adsorption. (d) and (e) correspond to the COOH* and HCOO* adsorbate structures, respectively.

conditions might correlate with the lower ΔG in the presence of a Cu vacancy, and a more rigorous account will be the subject of follow-up work. Due to the coexistence of the $NaInS_2$, we also calculated ΔG of the two CO_2R intermediates on the $NaInS_2$ (003) surface. With ΔG as low as -3 to -5 eV (*cf.* Table S3, ESI†), the binding of both COOH* and HCOO* is arguably too strong to enable an effective catalytic process. Therefore, we conclude that $NaInS_2$ is unlikely to be involved in the CO_2R catalytic process.

Conclusions

In summary, we showed that CIGS could be employed as a photocathode for direct semiconductor/electrolyte CO_2R in aqueous media. CIGS thin films yielded PEC CO_2R products like CO and HCOO- with a combined faradaic efficiency of >40% with stability over 80 min without the need for protection layers and co-catalysts. We showed the stability of CIGS under PEC CO_2R operation (-0.4 V *vs.* RHE and 0.1M $KHCO_3$ under illumination) using *operando* Raman spectroscopy, where the main A_1 mode of CIGS was unaffected. Using postmortem XPS analysis, we discovered the formation of hydroxides/oxides of In and Ga after PEC CO_2R operation, which could potentially lead to self-passivation of CIGS, improving its stability. Furthermore, the calculated adsorption energies for the HCOO* and carboxyl COOH* intermediate show that the possible binding sites are Ga and In, supporting postmortem XPS and XAS analysis that they might serve as the catalytic sites. More generally, our findings suggest that the previously unexplored Cu-deficient surface composition and specific surface defects, especially deep anti-site defects, might be playing a key role in governing the unique photoelectrochemical behavior of CIGS. PEC operation on the co-catalyst free CIGS surface leads to the possibility of a simple device architecture making additional coating layers redundant. The photocurrent density and faradaic efficiency can be improved by applying a suitable electron transport layer (ETL) and co-catalyst layer. However, it is not trivial, as it is extremely challenging to steer CO_2 reduction selectivity on semiconducting photocathodes, as also shown in a recent related study on Sb_2Se_3-based photocathodes. The bandgap tunability (variation in energy band positions) of CIGS through Ga alloying offers an advantage to further improve the PEC performance and tune the product selectivity. Looking forward, the stable performance of CIGS photocathodes for CO_2 reduction in aqueous media provides a rare opportunity to understand the complex catalytic process at the semiconductor–electrolyte interface and explore the role of light itself to change the reaction kinetics at the semiconducting surface. Furthermore, the endurance of the wide bandgap CIGS films and activity towards CO_2R opens a way forward towards higher order C_2 products by exploiting the rich defect chemistry and promoting C–C coupling on the CIGS surface.

Author contributions

Data availability

The data supporting this article have been included as part of the ESI.†

Conflicts of interest

There are no conflicts to declare.

Acknowledgements

References

1 P. B. Pati, R. Wang, E. Boutin, S. Diring, S. Jobic, N. Barreau, F. Odobel and M. Robert, *Nat. Commun.*, 2020, **11**, 3499.

2 J. M. C. M. Dela Cruz, Á. Balog, P. S. Tóth, G. Bencsik, G. F. Samu and C. Janáky, *EES Catal.*, 2024, **2**, 664–674.

3 J. Guerrero, E. Bajard, N. Schneider, F. Dumoulin, D. Lincot, U. Isci, M. Robert and N. Naghavi, *ACS Energy Lett.*, 2023, **8**, 3488–3493.

4 M. Xia, L. Pan, Y. Liu, J. Gao, J. Li, M. Mensi, K. Sivula, S. M. Zakeeruddin, D. Ren and M. Grätzel, *J. Am. Chem. Soc.*, 2023, **145**, 27939–27949.

5 B. Shan, S. Vanka, T.-T. Li, L. Troian-Gautier, M. K. Brennaman, Z. Mi and T. J. Meyer, *Nat. Energy*, 2019, **4**, 290–299.

6 J. Yu, X. Hao, L. Mu, W. Shi and G. She, *Chem. – Eur. J.*, 2024, **30**, e202303552.

7 K. Wang, Y. Ma, Y. Liu, W. Qiu, Q. Wang, X. Yang, M. Liu, X. Qiu, W. Li and J. Li, *Green Chem.*, 2021, **23**, 3207–3240.

8 J. Gu, A. Wuttig, J. W. Krizan, Y. Hu, Z. M. Detweiler, R. J. Cava and A. B. Bocarsly, *J. Phys. Chem. C*, 2013, **117**, 12415–12422.

9 J. Sun, N. Guijarro, P. Li, U. Thumu, J.-H. Yum, K. Sivula and Z. M. Wang, *ACS Appl. Nano Mater.*, 2023, **6**, 10106–10114.

10 G. Liu, F. Zheng, J. Li, G. Zeng, Y. Ye, D. M. Larson, J. Yano, E. J. Crumlin, J. W. Ager, L.-W. Wang and F. M. Toma, *Nat. Energy*, 2021, **6**, 1124–1132.

11 Y. Lai, N. B. Watkins, C. Muzzillo, M. Richter, K. Kan, L. Zhou, J. A. Haber, A. Zakutayev, J. C. Peters, T. Agapie and J. M. Gregoire, *ACS Energy Lett.*, 2022, **7**, 1195–1201.

12 S. Yoshino, A. Iwase, Y. Yamaguchi, T. M. Suzuki, T. Morikawa and A. Kudo, *J. Am. Chem. Soc.*, 2022, **144**, 2323–2332.

13 T. Takayama, K. Sato, T. Fujimura, Y. Kojima, A. Iwase and A. Kudo, *Faraday Discuss.*, 2017, **198**, 397–407.

14 T. Takayama, A. Iwase and A. Kudo, *ACS Appl. Mater. Interfaces*, 2024, **16**, 36423–36432.

15 T. Yoshida, A. Yamaguchi, N. Umezawa and M. Miyauchi, *J. Phys. Chem. C*, 2018, **122**, 21695–21702.

16 S. Ikeda, S. Fujikawa, T. Harada, T. H. Nguyen, S. Nakanishi, T. Takayama, A. Iwase and A. Kudo, *ACS Appl. Energy Mater.*, 2019, **2**, 6911–6918.

17 Y. Liu, M. Xia, D. Ren, S. Nussbaum, J.-H. Yum, M. Grätzel, N. Guijarro and K. Sivula, *ACS Energy Lett.*, 2023, **8**, 1645–1651.

18 S. Kim, T. Nagai, H. Tampo, S. Ishizuka and H. Shibata, *Prog. Photovolt.: Res. Appl.*, 2020, **28**, 816–822.

19 S. Shukla, M. Sood, D. Adeleye, S. Peedle, G. Kusch, D. Dahliah, M. Melchiorre, G.-M. Rignanese, G. Hautier, R. Oliver and S. Siebentritt, *Joule*, 2021, **5**, 1816–1831.

20 J. K. Larsen, K. V. Sopiha, C. Persson, C. Platzer-Björkman and M. Edoff, *Adv. Sci.*, 2022, **9**, 2200848.

21 Z.-K. Yuan, S. Chen, Y. Xie, J.-S. Park, H. Xiang, X.-G. Gong and S.-H. Wei, *Adv. Energy Mater.*, 2016, **6**, 1601191.

22 A. Karami, M. Morawski, H. Kempa, R. Scheer and O. Cojocaru-Mirédin, *Sol. RRL*, 2024, **8**, 2300544.

23 N. Berry, M. Cheng, C. L. Perkins, M. Limpinsel, J. C. Hemminger and M. Law, *Adv. Energy Mater.*, 2012, **2**, 1124–1135.

24 D. Rudmann, D. Brémaud, A. F. da Cunha, G. Bilger, A. Strohm, M. Kaelin, H. Zogg and A. N. Tiwari, *Thin Solid Films*, 2005, **480–481**, 55–60.

25 S. Shukla, D. Adeleye, M. Sood, F. Ehre, A. Lomuscio, T. P. Weiss, D. Siopa, M. Melchiorre and S. Siebentritt, *Phys. Rev. Mater.*, 2021, **5**, 055403.

26 N. Guijarro, M. S. Prévot, M. Johnson, X. Yu, W. S. Bourée, X. A. Jeanbourquin, P. Bornoz, F. Le Formal and K. Sivula, *J. Phys. D: Appl. Phys.*, 2017, **50**, 044003.

27 A. Neisser, I. Hengel, R. Klenk, T. W. Matthes, J. Álvarez-García, A. Pérez-Rodríguez, A. Romano-Rodríguez and M. C. Lux-Steiner, *Sol. Energy Mater. Sol. Cells*, 2001, **67**, 97–104.

28 Q. Cao, O. Gunawan, M. Copel, K. B. Reuter, S. J. Chey, V. R. Deline and D. B. Mitzi, *Adv. Energy Mater.*, 2011, **1**, 845–853.

29 T. Klinkert, B. Theys, G. Patriarche, M. Jubault, F. Donsanti, J. F. Guillemoles and D. Lincot, *J. Chem. Phys.*, 2016, **145**, 154702.

30 S. Merdes, D. Abou-Ras, R. Mainz, R. Klenk, M. C. Lux-Steiner, A. Meeder, H. W. Schock and J. Klaer, *Prog. Photovolt.: Res. Appl.*, 2013, **21**, 88–93.

31 S. Merdes, R. Mainz, J. Klaer, A. Meeder, H. Rodriguez-Alvarez, H. W. Schock, M. C. Lux-Steiner and R. Klenk, *Sol. Energy Mater. Sol. Cells*, 2011, **95**, 864–869.

32 H. Hiroi, Y. Iwata, S. Adachi, H. Sugimoto and A. Yamada, *IEEE J. Photovolt.*, 2016, **6**, 760–763.

33 H. Hiroi, Y. Iwata, K. Horiguchi and H. Sugimoto, *IEEE J. Photovolt.*, 2016, **6**, 309–312.

34 H. Hiroi, Y. Iwata, H. Sugimoto and A. Yamada, *IEEE J. Photovolt.*, 2016, **6**, 1630–1634.

35 G. He, C. Yan, J. Li, X. Yuan, K. Sun, J. Huang, H. Sun, M. He, Y. Zhang, J. A. Stride, M. A. Green and X. Hao, *ACS Appl. Energy Mater.*, 2020, **3**, 11974–11980.

36 H. Kaga, Y. Tsutsui, A. Nagane, A. Iwase and A. Kudo, *J. Mater. Chem. A*, 2015, **3**, 21815–21823.

37 J. J. Frick, R. J. Cava and A. B. Bocarsly, *Chem. Mater.*, 2018, **30**, 4422–4431.

38 Y. Liu, M. Bouri, L. Yao, M. Xia, M. Mensi, M. Grätzel, K. Sivula, U. Aschauer and N. Guijarro, *Angew. Chem., Int. Ed.*, 2021, **60**, 23651–23655.

39 N. Guijarro, M. S. Prévot, X. Yu, X. A. Jeanbourquin, P. Bornoz, W. Bourée, M. Johnson, F. Le Formal and K. Sivula, *Adv. Energy Mater.*, 2016, **6**, 1501949.

40 N. Gaillard, D. Prasher, M. Chong, A. Deangelis, K. Horsley, H. A. Ishii, J. P. Bradley, J. Varley and T. Ogitsu, *ACS Appl. Energy Mater.*, 2019, **2**, 5515–5524.

41 N. Barreau, E. Bertin, A. Crossay, O. Durand, L. Arzel, S. Harel, T. Lepetit, L. Assmann, E. Gautron and D. Lincot, *EPJ Photovolt.*, 2022, **13**, 17.

42 Y. Deng and B. S. Yeo, *ACS Catal.*, 2017, **7**, 7873–7889.

43 L. Choubrac, E. Bertin, F. Pineau, L. Arzel, T. Lepetit, L. Assmann, T. Aloui, S. Harel and N. Barreau, *Prog. Photovolt.: Res. Appl.*, 2023, **31**, 971–980.

44 S. Yuan, X. Wang, Y. Zhao, Q. Chang, Z. Xu, J. Kong and S. Wu, *ACS Appl. Energy Mater.*, 2020, **3**, 6785–6792.

45 A. Loubat, S. Béchu, M. Bouttemy, J. Vigneron, D. Lincot, J.-F. Guillemoles and A. Etcheberry, *J. Vac. Sci. Technol., A*, 2019, **37**, 041201.

46 F. Scharmann, G. Cherkashinin, V. Breternitz, C. Knedlik, G. Hartung, T. Weber and J. A. Schaefer, *Surf. Interface Anal.*, 2004, **36**, 981–985.

47 S. Béchu, M. Bouttemy, J.-F. Guillemoles and A. Etcheberry, *Appl. Surf. Sci.*, 2022, **576**, 151898.

48 C. L. Hinkle, M. Milojevic, B. Brennan, A. M. Sonnet, F. S. Aguirre-Tostado, G. J. Hughes, E. M. Vogel and R. M. Wallace, *Appl. Phys. Lett.*, 2009, **94**, 162101.

49 X. Yu, X. An, A. Shavel, M. Ibáñez and A. Cabot, *J. Mater. Chem. A*, 2014, **2**, 12317–12322.

50 Z. M. Detweiler, S. M. Wulfsberg, M. G. Frith, A. B. Bocarsly and S. L. Bernasek, *Surf. Sci.*, 2016, **648**, 188–195.

51 J. Li, Y. Ma, G. Chen, J. Gong, X. Wang, Y. Kong, X. Ma, K. Wang, W. Li, C. Yang and X. Xiao, *Sol. RRL*, 2019, **3**, 1800254.

52 F. Werner, B. Veith-Wolf, C. Spindler, M. R. Barget, F. Babbe, J. Guillot, J. Schmidt and S. Siebentritt, *Phys. Rev. Appl.*, 2020, **13**, 054004.

53 S. Garud, N. Gampa, T. G. Allen, R. Kotipalli, D. Flandre, M. Batuk, J. Hadermann, M. Meuris, J. Poortmans, A. Smets and B. Vermang, *Phys. Status Solidi A*, 2018, **215**, 1700826.

54 F. Werner, B. Veith-Wolf, M. Melchiorre, F. Babbe, J. Schmidt and S. Siebentritt, *Sci. Rep.*, 2020, **10**, 7530.

55 J. P. Perdew, M. Ernzerhof and K. Burke, *J. Chem. Phys.*, 1996, **105**, 9982–9985.

56 C. Adamo and V. Barone, *J. Chem. Phys.*, 1999, **110**, 6158–6170.

57 G. Kresse and J. Furthmüller, *Comput. Mater. Sci.*, 1996, **6**, 15–50.

58 G. Kresse and J. Furthmüller, *Phys. Rev. B: Condens. Matter Mater. Phys.*, 1996, **54**, 11169–11186.

59 S. Grimme, J. Antony, S. Ehrlich and H. Krieg, *J. Chem. Phys.*, 2010, **132**, 154104.

60 A. Zunger, S. H. Wei, L. G. Ferreira and J. E. Bernard, *Phys. Rev. Lett.*, 1990, **65**, 353–356.

61 X. Zheng, P. De Luna, F. P. García de Arquer, B. Zhang, N. Becknell, M. B. Ross, Y. Li, M. N. Banis, Y. Li, M. Liu, O. Voznyy, C. T. Dinh, T. Zhuang, P. Stadler, Y. Cui, X. Du, P. Yang and E. H. Sargent, *Joule*, 2017, **1**, 794–805.

62 R. Kortlever, J. Shen, K. J. P. Schouten, F. Calle-Vallejo and M. T. M. Koper, *J. Phys. Chem. Lett.*, 2015, **6**, 4073–4082.

63 J. K. Nørskov, J. Rossmeisl, A. Logadottir, L. Lindqvist, J. R. Kitchin, T. Bligaard and H. Jónsson, *J. Phys. Chem. B*, 2004, **108**, 17886–17892.

64 atomote2: **https://github.com/materialsproject/atomate2**.

65 A. S. Rosen, *et al.*, Jobflow: Computational Workflows Made Simple, *J. Open Source Softw.*, 2024, **9**(93), 5995, DOI: **10.21105/joss.05995**.